Catalysis Science & Technology

ROYAL SOCIETY OF CHEMISTRY

PAPER

View Article Online
View Journal

Cite this: DOI: 10.1039/d6cy00135a

Adsorption or photocatalysis? Engineering BiOI with metalorganic framework CAU-17 and microporous organic polymer MOP-CH_2EDA to enhance ciprofloxacin removal from water

Sepideh G. Khasevani,[a] Saulius Kaciulis,[b] Alessio Mezzi,[b] Shokat Sarmad,[c] Jyri-Pekka Mikkola,[cd] Dariush Nikjoo[a] and Isabella Concina *[a]

This work reports the design of binary and ternary BiOI-based composites incorporating the metal–organic framework CAU-17 and the amine-functionalized microporous organic polymer MOP-CH_2EDA for the removal of ciprofloxacin (CIP) from water. The materials were synthesized *via* an *in situ* solvothermal approach and systematically characterized to establish structure–property relationships. The results reveal that adsorption and photocatalysis act as coupled and sequential processes, rather than independent pathways, with the polymer component enhancing CIP pre-concentration and the BiOI/MOF interface governing photodegradation. The ternary composite BCM-10% exhibited the best performance, achieving up to 80% CIP removal under simulated solar irradiation. Scavenger experiments indicate that $\cdot O_2^-$ is the dominant reactive species, while photogenerated holes also contribute significantly. The degradation process is strongly influenced by pH, reflecting the interplay between catalyst surface properties, reactive oxygen species generation, and CIP speciation. HPLC-MS analysis confirms the formation of multiple intermediates and highlights the complexity of the degradation pathways. Despite the improved performance of the ternary composites, the overall activity remains moderate compared to state-of-the-art photocatalysts, underscoring the limitations of current BiOI-based systems. The results emphasize that apparent kinetic behavior is strongly affected by adsorption contributions, complicating direct comparison with literature data. This study provides new insight into the design of multifunctional materials for water treatment, highlighting the importance of adsorption–photocatalysis synergy and the need for more rigorous and standardized evaluation of photocatalytic systems.

Received 2nd February 2026,
Accepted 13th May 2026

DOI: 10.1039/d6cy00135a

rsc.li/catalysis

1. Introduction

The widespread presence of antibiotics in natural waters has emerged as a critical environmental challenge over the past decade. Pharmaceuticals such as fluoroquinolones, macrolides, and sulfonamides are frequently detected in surface and groundwaters due to their extensive medical and agricultural use and limited biodegradability.[1,2] Among them, ciprofloxacin (CIP), a second-generation fluoroquinolone, is particularly persistent and retains biological activity even at trace concentrations.[3] Continuous exposure of microbial communities to such residues promotes the emergence of antibiotic-resistant bacteria and resistance genes, posing a serious risk to ecosystems and human health.[4,5]

Advanced oxidation processes (AOPs) have attracted considerable attention for the degradation of recalcitrant organic pollutants owing to their capability to generate highly reactive oxygen species (ROS) such as $\cdot OH$, $\cdot O_2^-$, and h^+, which can non-selectively mineralize complex molecules.[6–8] Among visible-light-responsive semiconductors, bismuth oxyhalides (BiOX, X = Cl, Br, I) have attracted significant attention due to their unique layered structure, consisting of alternating $[Bi_2O_2]^{2+}$ slabs and halide layers, which generate an internal electric field promoting charge separation.[9–11] In particular, BiOI exhibits a narrow bandgap (1.7–2.4 eV), allowing efficient solar-light absorption; however, its practical application is limited by rapid electron–hole recombination and moderate photocatalytic efficiency.[12,13] To overcome these limitations, BiOI is often combined with secondary

[a] *Department of Engineering Sciences and Mathematics, Luleå University of Technology, 97187 Luleå, Sweden. E-mail: isabella.concina@ltu.se*
[b] *Institute for the Study of Nanostructured Materials, ISMN-CNR, 00015 Monterotondo Stazione, Roma, Italy*
[c] *Technical Chemistry, Department of Chemistry, Chemical-Biological Centre, Umeå University, SE-90871 Umeå, Sweden*
[d] *Industrial Chemistry & Reaction Engineering, Johan Gadolin Process Chemistry Centre, Åbo Akademi University, FI-20500 Åbo-Turku, Finland*

components to improve charge separation, extend light absorption, or introduce additional functionalities. Strategies include coupling with metal–organic frameworks (MOFs), carbon materials, or conductive polymers.[14–22]

In parallel with photocatalysis, adsorption has gained attention as an effective and energy-efficient strategy for antibiotic removal.[22–25] Adsorption allows the pre-concentration and partial elimination of contaminants before light-driven oxidation.[26] Materials with tunable surface chemistry and porosity, including MOFs and microporous organic polymers (MOPs), offer high surface areas and tunable surface chemistries, allowing strong interactions with organic contaminants through hydrogen bonding, electrostatic forces and π–π interactions.[27–32]

In this context, integrating adsorption and photocatalysis within a single multifunctional material represents a promising strategy to enhance pollutant removal efficiency.

Based on these considerations, this study explores the design of binary and ternary composites based on BiOI, the aluminum-based MOF CAU-17, and an amine-functionalized microporous organic polymer (MOP-CH_2EDA). BiOI was selected as the visible-light-active component, while CAU-17 was introduced to promote heterojunction formation and improve charge separation. The incorporation of MOP-CH_2EDA aims to enhance adsorption through specific interactions with ciprofloxacin, thereby increasing its local availability at reactive sites. Compared to conventional systems that primarily optimize electronic properties (*e.g.*, doped BiOI or BiOI/carbon composites), this approach seeks to simultaneously control light absorption, charge transfer, and pollutant pre-concentration.

The objective of this work is therefore not only to improve CIP removal efficiency, but also to elucidate the interplay between adsorption and photocatalysis in such multifunctional systems. By systematically varying the composition of BiOI/MOF/MOP composites and combining structural and kinetic analyses, this study aims to provide deeper insight into the role of interfacial engineering in photocatalytic water treatment and to highlight the complexity of processes governing antibiotic degradation.

2. Experimental section

2.1. Materials synthesis

All precursors (ACS reagent, ≥98%) for the synthesis of the composites were purchased from Sigma-Aldrich. CIP was purchased from ACROS. All chemicals were used without any further purification.

2.1.1. Synthesis of BiOI. $Bi(NO_3)_3{\cdot}5H_2O$ (0.98 g) was dissolved in 15 ml of ethylene glycol (EG) under vigorous stirring for 30 min. In another beaker, KI (0.33 g) was dissolved in 15 ml of EG under stirring for 30 min. The obtained KI solution was added dropwise to the $Bi(NO_3)_3{\cdot}5H_2O$ solution, under continuous stirring, for 30 min. The reaction mixture was then transferred to a stainless-steel autoclave lined with Teflon and heated at 130 °C for 18 h. The precipitate was washed three times with distilled water and ethanol and subsequently dried in an oven at 60 °C. For a detailed discussion of the synthesis, the reader is referred to ref. 33.

2.1.2. Synthesis of polyamine-tethered MOP (MOP-CH_2-EDA). The MOP-CH_2EDA was synthesized based on previous literature.[34] Briefly, Friedel–Crafts self-condensation was used to synthesize a series of MOPs with hyper-crosslinked structures. A MOP was synthesized based on the copolymerization of α,α-dichloro-*p*-xylene (*p*-DCX). The monomer, *p*-DCX was added to anhydrous dichloroethane (DCE, 5 mL) under a nitrogen atmosphere. A slurry of iron(III) chloride ($FeCl_3$, 0.7 g,) in DCE (5 ml) was then added. The mixture was heated at 353 K and kept under stirring for 18 h under a nitrogen atmosphere. The obtained brown precipitate was washed in a Soxhlet extractor with methanol until the filtrate became clear and finally dried in an oven at 60 °C for 24 h. 200 mg of the MOP were dispersed in a mixture of paraformaldehyde (1.0 g), glacial acetic acid (6.0 mL), H_3PO_4 (3.0 mL), and concentrated HCl (20 ml). The resultant mixture was heated at 90 °C in an oil bath and kept under reflux for 3 days. The collected solid was washed with water and methanol and then dried at 60 °C under a vacuum for 8 h. The dried brown powder (200 mg) was dispersed in 20 ml of ethylenediamine (EDA) and heated to 90 °C in an oil bath for 3 days. The resulting solid was collected, washed with distilled water and methanol, and then dried in a vacuum oven for 8 h.

2.1.3. *In situ* synthesis of BiOI/CAU-17 composites. For the *in situ* synthesis of the binary BC composite, 0.56, 0.11, and 0.16 g of CAU-17 (10, 20, 30 wt% with respect to BiOI) were ultrasonically dispersed into 5 ml of methanol and 15 ml of DMF, respectively, followed by the addition of 0.98 g $Bi(NO_3)_3{\cdot}5H_2O$. A solution of 0.33 g of KI in 15 ml EG was then added dropwise into the solution under magnetic stirring. Subsequently, the reaction mixture was transferred into a Teflon-lined stainless-steel autoclave and kept at 130 °C for 18 h. Finally, the resulting precipitates with different amounts of CAU-17 were washed with ethanol and distilled water several times and dried in an oven at 80 °C for 8 h.

2.1.4. Synthesis of BiOI/CAU-17/MOP-CH_2EDA (BCM-5, 10, 15%). The ternary composites BiOI/CAU-17/MOP-CH_2EDA (hereafter BCM) were prepared as follows. 0.033 g, 0.067 g, and 0.1 g of MOP-CH_2EDA (5, 10, 15 wt% with respect to BiOI, respectively) were dispersed in a mixture of 15 ml methanol and 5 ml DMF under sonication for 15 min. $Bi(NO_3)_3{\cdot}5H_2O$ (0.48 g) and H_3BTC (0.63 g mmol) were then added. The resultant mixture was transferred in a Teflon-lined stainless-steel autoclave and heated at 120 °C for 24 h. Finally, the collected solids were washed with methanol and DMF and dried in an oven at 80 °C. The dried grey powder was dispersed in 15 ml of EG and sonicated for 20 min, and then 0.98 g of $Bi(NO_3)_3{\cdot}5H_2O$ in EG was added to the above solution under magnetic stirring for 1 h. In another beaker, KI (0.33 g) was dissolved in 15 ml of EG under stirring for 30 min and then poured into the above solution, which was then kept under stirring for 2 h. The resulting precursor suspension was poured into a Teflon-lined stainless-steel autoclave and kept at 130 °C for 18 h. The products were

repeatedly washed with distilled water and ethanol and dried overnight in an oven at 80 °C.

2.2. Materials characterization

X-Ray Diffraction (XRD) analysis was carried out in a PANalytical Empyrean instrument equipped with a PIXcel3D detector using Cu-Kα radiation at 40 kV and 45 mA settings. A Bruker VERTEX 80v FTIR spectrometer was used to record the infrared spectra of the samples, in the range 4000–500 cm^{-1}. Spectra were collected in transmittance mode (with a resolution of 4 cm^{-1}) by preparing KBr pellets.

The morphological analysis of the materials was performed with a JSM-IT300 scanning electron microscope (SEM) equipped with an energy-dispersive X-ray spectroscopy (EDX) detector. Thermogravimetric analysis (TGA) was performed using a STA 449C Jupiter (NETZSCH, Germany) instrument under Ar flow from 20 to 700 °C at a heating rate of 10 °C min^{-1}. Brunauer–Emmett–Teller (B.E.T.) surface area and porosity of materials were analyzed with a Micrometrics Gemini V 2390 apparatus (Micromeritics, Norcross GA, USA). The samples were degassed under vacuum (1×10^{-4} Pa) at 363 K for 24 h before measurement. Diffuse reflectance spectroscopy (DRS) analysis of the samples was recorded in Agilent Cary5000 spectrophotometer. X-ray photoelectron spectroscopy (XPS) was carried out by using a spectrometer Escalab 250Xi (Thermo Fisher Scientific Ltd., UK) with monochromatic Al Kα X-ray source in standard electromagnetic lens mode (diameter of analyzed area of about 1 mm) at constant pass energy of 50 eV. All experimental data were acquired and processed by using Avantage v.5 software (Thermo Fisher Scientific Ltd., UK). The "smart" background and mixed Lorentzian/Gaussian peak shape was used for the peak fitting routine. Scofield's relative sensitive factors with energy compensation coefficient of $KE^{0.6}$ were applied for the elemental quantification.

2.3. Adsorption and photocatalytic tests

Adsorption of CIP under dark was evaluated by dispersing 10 mg of catalyst in a 100 ml CIP (10 mg L^{-1}) aqueous solution and stirring the mixture for 120 min. Aliquots (3 ml) of the reaction mixture were taken out periodically, centrifuged (4000 rpm, 15 min) and analyzed through spectrophotometry.

Photocatalytic performance of the materials was investigated under dark and solar-simulated light (AM 1.5G solar simulator, calibrated with a silicon reference cell to an irradiance of 100 mW cm^{-2}). 10 mg of catalyst were dispersed in a 100 ml CIP (10 mg L^{-1}) aqueous solution. To reach the adsorption/desorption equilibrium, the reaction mixture was magnetically stirred in dark at room temperature for 30 min. During irradiation, 3.0 ml of the suspension was taken out of the reaction mixture at fixed times. CIP concentration was quantified through spectrophotometry using the CIP absorption peak at 273 nm. The pH of the reaction mixture was modulated by adding either HCl or NaOH for pH-related tests.

The reaction course was evaluated by studying the relative change of CIP concentration (C_t/C_0) over time.

The following equation was applied to determine the degradation efficiency:

$$X\% = \frac{C_0 - C(t)}{C_0} \times 100$$

For the recycling experiments, the previously used BCM-10% photocatalyst was centrifuged out of the solution, dried in an oven at 80 °C for 8 h, and then reused to degrade CIP at the same concentration.

2.4. High performance liquid chromatography coupled with mass spectrometry (HPLC-MS)

For HPLC-MS analysis, a LCQ FLEET ion-trap mass spectrometer (Thermo Finnigan) was employed. Electrospray ionization was performed using an AJS-ES source operating in both positive and negative modes. The source conditions were as follows: capillary voltage 1300 V, nozzle voltage 2000 V, gas temperature 250 °C, sheath gas temperature 350 °C, drying gas flow 12.0 L min^{-1}, sheath gas flow 12.0 L min^{-1}, and nebulizer pressure 35 psig. The fragmentor voltage was set to 70 V. Data acquisition was conducted in full-scan mode, and no MS/MS experiments were performed. Further, mass spectra were acquired over a scan range of m/z 100–1000 in both positive and negative ionization modes. No selected ion monitoring (SIM) was applied.

An adequate amount of the reaction mixture (10 μL) was injected into the HPLC column (Hypersil gold C18, 2.1 × 50 mm with 1.9 μm particle size) by applying an auto-injector (Thermo Finnigan). In the mobile phase, a combination of acetonitrile (solvent A) and water (solvent B) was used, both of the solvents containing 0.1% (v/v) formic acid. The mobile phase gradient is reported in Table 1.

3. Results and discussion

3.1. Structural, morphological and textural characterization

XRD patterns of the prepared materials are presented in Fig. S1 (SI), while the corresponding lattice parameters and crystallite sizes are summarized in Table 2. All diffraction peaks can be indexed to the tetragonal phase of BiOI (JCPDS 10-0445), confirming the preservation of BiOI structure in the both binary and ternary composites. For pure BiOI, the unit cel parameters were determined $a = b = 3.98$ Å and $c = 9.58$ Å. In the composites, the lattice vectors a and b remained essentially

Table 1 Gradient of the mobile phase

Time (min)	Solvent A : solvent B (% vol : vol)	Flow rate (μL ml^{-1})
0–1.7	5 : 95	250
1.7–8	30 : 70	350
8–10	100 : 0	350
10–12	5 : 95	250

Table 2 Structural parameters extracted from XRD analysis

Sample	Unit cell parameters (Å)	Crystallite sizes (nm)
BiOI	$a = b = 3.98$ $c = 9.58$	9.31
BC-10%	$a = b = 3.98$ $c = 9.76$	6.65
BC-20%	$a = b = 3.96$ $c = 9.89$	6.09
BC-30%	$a = b = 3.94$ $c = 10.16$	5.41
BCM-5%	$a = b = 3.96$ $c = 9.89$	4.77
BCM-10%	$a = b = 4.00$ $c = 10.16$	6.66
BCM-15%	$a = b = 3.96$ $c = 10.15$	8.51

unchanged, whereas the c vector shows a clear dependence on composition (Fig. 1a). In particular, the interlayer distance between the $[Bi_2O_2]^{2+}$ slabs increased progressively with increasing CAU-17 content, indicating structural expansion along the stacking direction. This trend was accompanied by a reduction in crystallite size (Fig. 1b), suggesting the CAU-17 promotes the formation of smaller BiOI domains.

This behaviour can be attributed to the role of CAU-17 during the *in situ* synthesis, where it likely acts as a. nucleation platform, providing dispersed growth sites that limit crystal coalescence. In contrast, the incorporation of MOP-CH_2EDA leads to a monotonic increase in crystallite size (Fig. 1b), indicating a different interaction with the growing BiOI phase, possibly favoring crystal growth or aggregation.

It should be noted that no peak ascribable to the crystalline structure of CAU-17 (that was successfully prepared, as confirmed by XRD analysis displayed in Fig. S1 in the SI) was observed in the XRD of the composite materials: this was previous reported and can be ascribed to the high dispersibility of CAU-17 in the BiOI matrix.[35]

The last remark concerns the reflection pertaining to (001) plane, only visible in the pattern of pure BiOI, indicating that this facet is less or not at all exposed in the composites.[36]

SEM analysis of pure samples BiOI, CAU-17, MOP-CH_2-EDA, and the binary and ternary composites is reported in Fig. 2. BiOI presented a microsphere structure, with an average size of 1.6 ± 0.2 μm, with a spongy surface consisting of small lamellae (Fig. 2a and b). CAU-17 featured an elongated, rod-like structure (Fig. 2c), as previously reported,[37] while MOP-CH_2EDA (Fig. 2d) showed an irregular structure, typical for amorphous materials. In both the binary and ternary composites (Fig. 2e–g), the elongated CAU-17 structures are covered by BiOI microspheres in a rather conformal way, although their end is shown protruding outside the composite. The MOP-CH_2EDA was observed as incorporated in the overall structure of the ternary composite (Fig. 2g).

B.E.T. analysis was used to quantify the specific surface area, pore volume and pore average size of the prepared materials (results are plotted in Fig. 3 and reported in Table S1 in the SI). A high surface area is an asset for a catalyst, potentially favoring both a superior adsorption capacity of the material and the presence of a high number of catalytically active sites. The N_2 adsorption–desorption isotherms (showed in Fig. S2 in the SI) of all samples showed

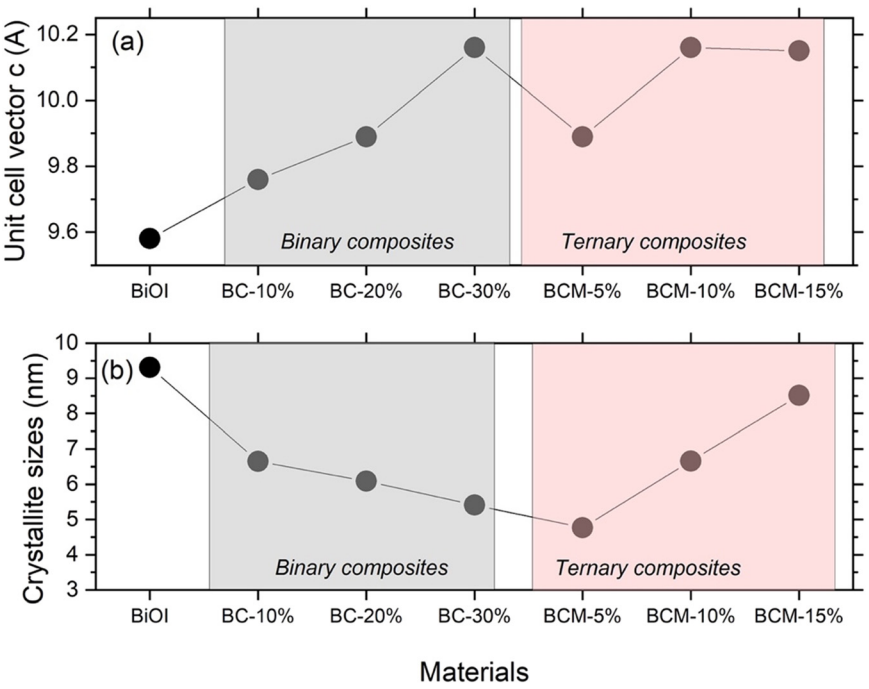

Fig. 1 Unit cell vector *c* (a) and crystallite sizes (b) of the prepared materials.

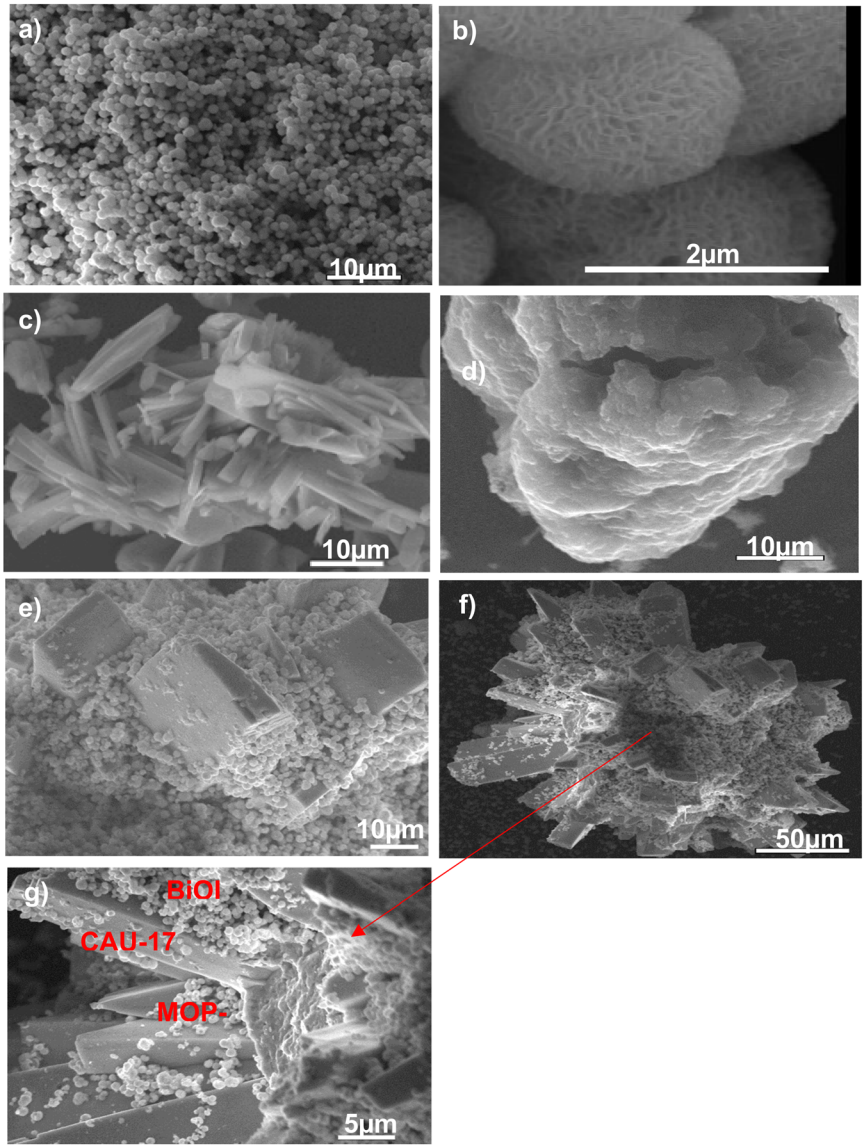

Fig. 2 Scanning electron micrographs of the prepared materials. (a) and (b): BiOI; (c): CAU-17; (d): MOP-CH_2EDA; (e): BC-20%; (f) and (g) BCM-10%.

a typical type IV behavior, attributed to the mesoporous structure.

The average pore volume of both binary and ternary composites showed a clear dependence on material composition (Fig. 3c and d). Increasing the content of CAU-17 led to a progressive decrease in pore volume, consistent with partial pore blocking or structural densification. In contrast, the incorporation of MOP-CH_2EDA partially counteracts this effect within the ternary series, resulting in an increase in pore volume compared to the corresponding binary composites. Nevertheless, the *in situ* synthesis route overall led to lower pore volumes in the ternary materials relative to the BC series. The average pore size (Fig. 3e and f) did not vary significantly across the investigated samples, although a trend similar to that observed for pore volume can be identified. It should be noted, however, that for narrow mesopores (<10 nm), the BJH method may underestimate pore size by up to 20–30%, as continuum-based assumptions become less reliable at this scale.[38,39]

3.2. Spectroscopy characterization

FTIR analysis (reported in Fig. S3 and Table S2 in the SI) confirmed the formation of Bi–O and Bi–I bonds in pure BiOI,[40–42] as well as in CAU-17,[43,44] which also showed bands pertaining to the stretching of the aromatic ring and the stretching and bending of carboxylate units, as expected.

The characteristics vibrations of both BiOI and CAU-17 were found also in the binary BC-20% and ternary BCM-10% materials (whose spectra are reported in Fig. S3 in the SI as representative for the composites), confirming their successful preparation.

Diffuse reflectance spectroscopy (DRS) was used to analyze the response to light of the prepared materials and evaluate their optical bandgap (Fig. 4a and b). This latter, coupled

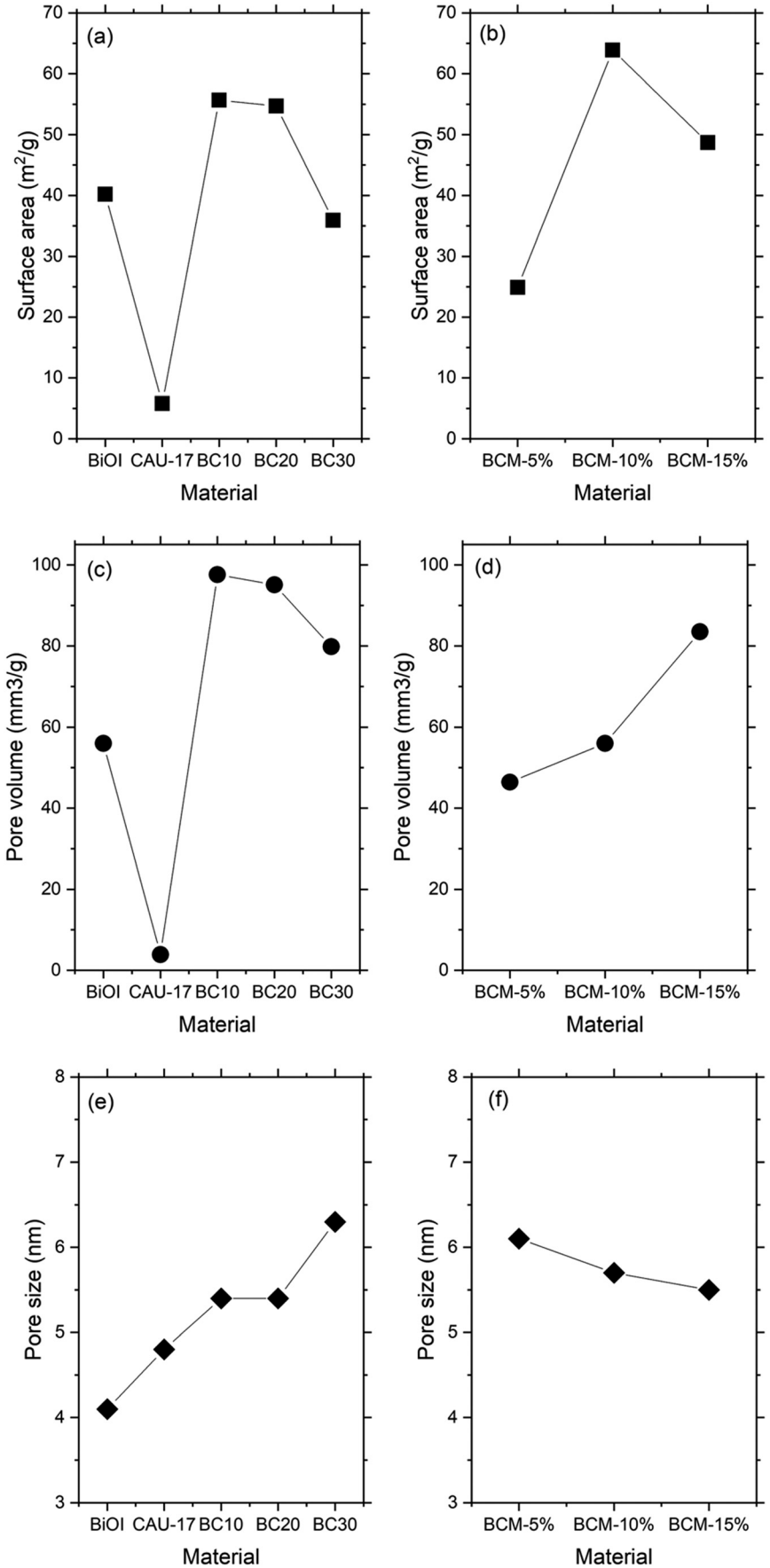

Fig. 3 Results of B.E.T. analysis plotted *vs.* material identity. (a), (c) and (e) surface area, pore volume and average pore size for bare materials and binary composites; (b), (d) and (f): surface area, pore volume and average pore size for ternary composites. Per each pair of plots, the scale on *Y*-axis is the same.

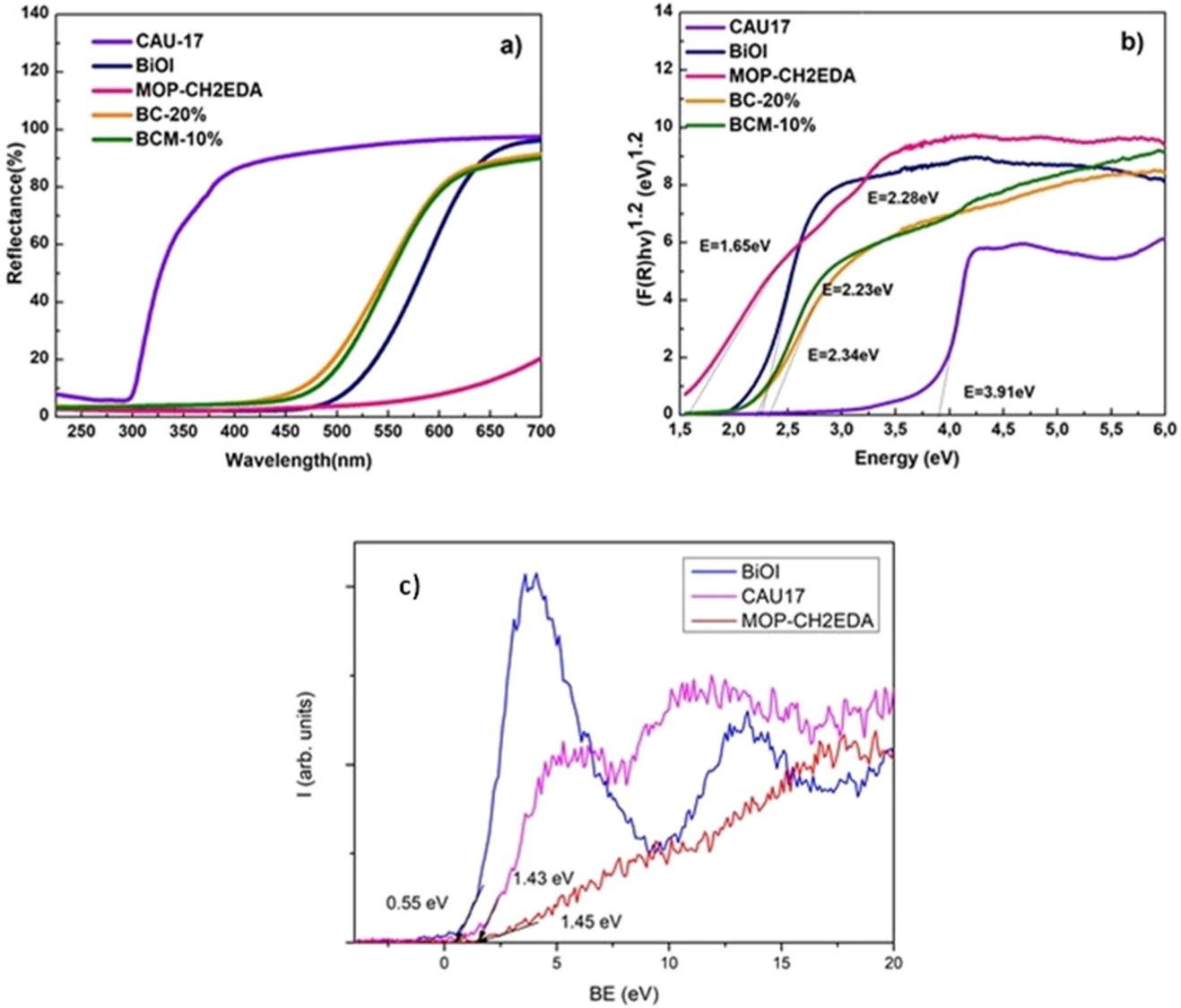

Fig. 4 (a) Diffuse reflectance spectra of the prepared materials; (b) Tauc plot; (c) XPS valence band spectra with VBM values.

with XPS spectra of the valence band to determine the position of valence band maximum (VBM), shown in Fig. 4c, allowed us to also calculate the position of the conduction band (quantitative results reported in Table 2). CAU-17 had an absorption limited to the UV region, while BiOI and MOP-CH_2EDA extended to the visible part of the EM spectrum (till 500 and 600 nm, respectively).[45,46] Compared to the absorption of CAU-17, DRS results indicated that the fabrication of the composites is beneficial in terms of extending the native absorption to the visible, which is desirable property when irradiating with simulated solar light. Fig. 4b shows the graph $(F(R)h\nu)^{1/2}$ *vs.* photon energy, used to estimate the optical bandgap energy.[47,48] The valence band maximum is then determined from XPS spectra. The equation: $E_{CB} = E_{VB} - Eg$ is used to calculate the conduction band (CB) position, where E_{VB} is the valence band position and Eg is the band gap, according to the energy scale of Fermi level at 0 eV.

Fig. S4 and S5 in the SI show the most important XPS results pertaining to Bi 4f and C 1s spectra, respectively, including their peak fittings. Only the chemical state Bi^{3+} was detected in the pure BiOI sample (Fig. S4a), which can be attributed to Bi_2O_3 and/or BiI_3. The quantification of XPS data (reported in Table S3 in the SI) that both compounds are present.

In the sample CAU-17, the spectrum of Bi 4f is composed of two contributions (Fig. S4b): an oxide component A at BE = 159.8 eV and a second component (B) at BE = 161.8 eV, which can be assigned to Bi in organic complex, similar to Bi acetate.[49]

The spectra of C 1s region, presented in Fig. S5, consists of 3 contributions for bare BiOI, and of 4 contributions for the samples CAU-17 and MOP-CH_2EDA. The first three components have identical BE values in all the samples, and are attributed to: aliphatic carbon (A) at 285.0 eV, bonds C–O (B) at 286.4–286.7 eV and carboxylic bonds –C═O (C) at 288.6–

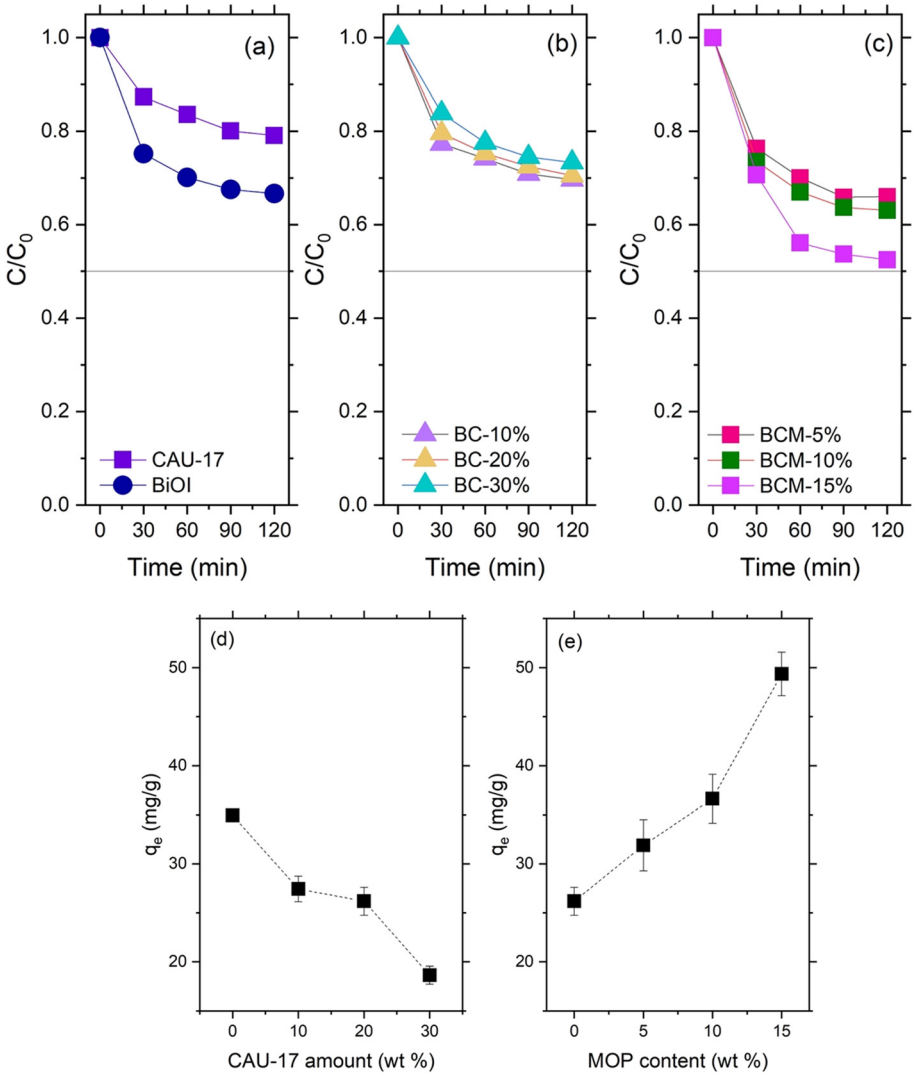

Fig. 5 (a), (b) and (c): CIP adsorption course for the materials under investigation. (d) and (e): Adsorption at the equilibrium for (a) the binary composites BiOI/CAU-17 and (b) the ternary composites BiOI/CAU-17/MOP-CH_2-EDA. Sample BC-20% is used as the reference for the zero-MOP content in plot (b). Markers are experimental points, lines are guide for the eye.

288.8 eV, but their intensities are varying (see the quantification in the SI). The fourth component D at BE = 291.1 eV corresponds to low content of contamination with carbonates.

3.3. Removal of ciprofloxacin: adsorption and photocatalysis

Fig. 5 shows the adsorption performance of the investigated materials toward CIP under dark over a 2 h period (the outcomes are summarized in Table 3). Bare BiOI exhibited a fair adsorption capacity, removing about 30% of the initial CIP amount in 30 min (Fig. 5a). The incorporation of CAU-17 led to a gradual decrease in absorption performance, with the binary composites showing reduced uptake as the MOF content increased (Fig. 5b), likely due to partial coverage of the active BiOI sites and reduced accessibility. In contrast, the introduction of MOP-CH_2EDA restored and enhanced the adsorption capacity (Fig. 5c). Increasing the polymer content resulted in progressively higher CIP uptake, with the ternary composites achieving removal of nearly 50% of the initial antibiotic concentration.

Table 3 Energy gap, valence band, and conduction band energies as retrieved from DRS and XPS analyses

Sample	Band gap (eV)	XPS valence band maximum (eV)	Conduction band position (eV)
BiOI	2.28	0.55 eV	−1.73
CAU-17	3.91	1.43 eV	−2.48
MOP-CH_2EDA	1.65	1.45 eV	−0.20

The adsorption kinetics of bare BiOI and CAU-17, as well as those of ternary composites, followed a pseudo-second order (PSO) model,[50] described by the equation:

$$\frac{t}{q_t} = \frac{1}{k_2 q_e^{\,2}} + \frac{t}{q_e} \quad (1)$$

where t is the reaction time, q_e the adsorption at the equilibrium, k_2 the adsorption kinetic constant and q_t the adsorption at time t. This latter is calculated according to:

$$q_t = \frac{(C_0 - C_t)V}{m} \quad (2)$$

In eqn (2), C_0 and C_t (in mg L^{-1}) are the CIP concentration at the beginning of the experiment and at a given t time, respectively, V (liters) is the volume of the solution and m (in grams) is the mass of the adsorber.

When PSO model is applicable, the rate of absorption depends on the availability of adsorption sites on the adsorbent (and not on the molecules of adsorbate): this parameter is then ruling the adsorption course when bare materials and ternary composites are considered.

However, adsorption kinetics of the binary composites behave differently and obey models for intraparticle diffusion.[51] Specifically, BC-10% and BC-20% obeyed a Weber & Morris model,[52] according to:

$$q_t = k_{WM} t^{1/2} \quad (3)$$

where k_{WM} is the kinetic constant according to Weber & Morris. This indicates that intraparticle diffusion controls the process. BC-30%, instead, showed a more complex behaviour, the adsorption curve being composed of two different contributions and obeying a two-regimes kinetics, according to:[53]

$$q_t - q_{t=t_1} = \frac{k_2}{(t - t_1)^{1/2}} \quad (4)$$

where t_1 is the time when the equilibrium of intraparticle diffusion is reached and after which it is broken.

We found a clear correspondence relating materials composition and adsorption capability (Fig. 5d and e), which clarifies the role of the additives in modifying the BiOI action as an adsorber. Insertion of CAU-17 causes a monotonic decrease in the value of the adsorption at the equilibrium, while the addition of MOP-CH_2-EDA results in a fair (monotonic) increase of this parameter. The ternary composite featuring 15% MOP amount could increase the q_e by about 43%, as compared to bare BiOI and by about 53% with respect to BC-20% from which it was synthesized. This ternary composite could adsorb almost 50% of the initial CIP amount present in the reaction mixture.

As said, bare materials and ternary composites were found to obey a pseudo-second order kinetic model: this indicates that the availability of adsorption sites rules their behavior as adsorbers.[54] The dependence of the adsorption properties of the binary composites on the diffusion of the adsorbate molecules in the materials pores suggests that the presence of CAU-17 hinders this mass transfer process, which is coherent with the very reduced pore volume measured by nitrogen physisorption (B.E.T.).

We then investigated the photocatalytic degradation of CIP under simulated solar light (Fig. 6). CAU-17 showed a poor catalytic activity (less than 20% of the initial CIP concentration was removed in 4 hours reaction time), while unmodified BiOI could degrade slightly more than 30% in the same time span. In both cases, we observed a plateau after 210 min, indicating that both materials stopped being active catalysts. The binary composite BC-30% showed similar performance as compared with BiOI and will be no longer discussed. Better catalytic skills were, instead, observed for the binary composites featuring 10% and 20% CAU-17, which could remove about 50% of the original CIP amount.

Based on this result, BC-20% was used to prepare the ternary composites including MOP-CH_2EDA.

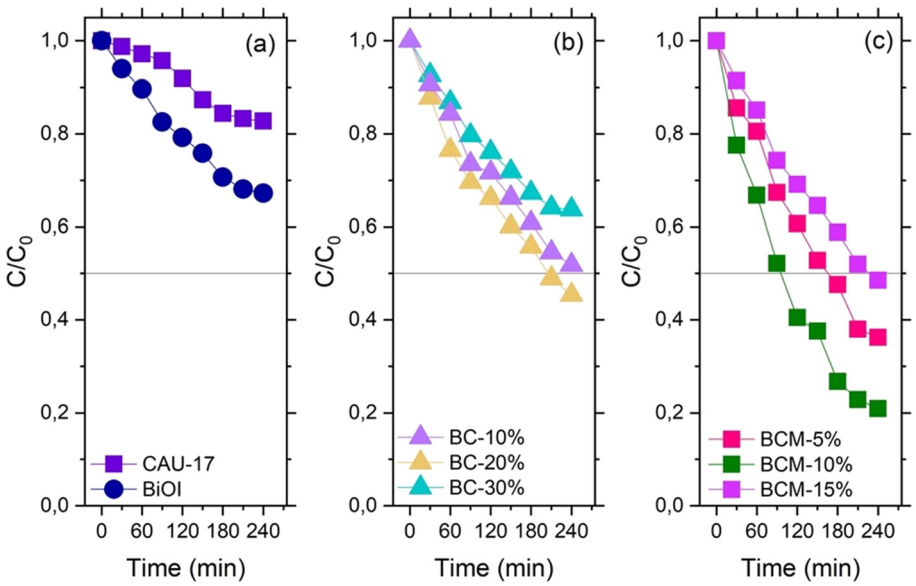

Fig. 6 CIP photocatalytic degradation supported by (a) bare materials, (b) binary and (c) ternary composites. A reference line identifying half the initial CIP concentration is drawn in each graph. Markers are experimental points, lines are guide for the eye.

The photocatalytic performance of the ternary composites under simulated solar irradiation is shown in Fig. 6 c. Among them, BCM-10% exhibited the highest activity, achieving approximately 80% CIP degradation after 240 min, while BCM-5% and BCM-15% reached about 64% and 56%, respectively. Overall, all ternary composites outperform the corresponding binary systems, indicating that the incorporation of MOP-CH_2-EDA positively contributes to photocatalytic performance. Table 4 reports the outcomes of adsorption and photocatalysis performance of the investigated materials.

However, no direct correlation could be established between degradation efficiency and a single material property, such as surface area or crystallite size. This observation underscores the complex and multiparametric nature of CIP photodegradation, where multiple factors—including adsorption behavior, charge separation, and interfacial interactions—simultaneously influence the overall performance. The improved activity of the composites compared to the bare materials (BiOI and CAU-17) can be partly attributed to the broader light absorption range, as evidenced by DRS analysis, as well as to the synergistic interplay between their structural and functional components.

It is also very relevant to observe that the fabrication of composites associates with a change in the reaction order. We indeed analyzed in more detail the reaction course of CIP degradation when pure materials and ternary composites were used, in the attempt to unveil the reaction kinetic order under irradiation (the results are reported in Fig. S8 in the SI). We tried a linearization procedure for the original experimental points, by plotting them as $-\ln\frac{C_t}{C_0}$, finding different trends for different catalytic materials. The experimental points were correlated through linear, exponential, and sigmoidal models, according to eqn (1)–(3) reported in the SI (obtained parameters have been summarized in Table S8).

CIP degradation by CAU-17 and BiOI displayed a sigmoidal trend under irradiation, while the curves pertaining to BCM composites could be well fitted by pseudo-first-order equations. The sigmoidal trend recorded for BiOI and CAU-17 catalysts are associated with an auto-catalytic reaction, indicating that some reaction product was possibly already present in the mixture at the beginning of the test under light irradiation (Fig. S8(a–d) and Table S8 in the SI).

BCM-5% obeys pseudo-first-order kinetics, but the C/C_0 *versus* time curve could not be well correlated with an exponential equation, casting doubt on the kinetic order (Fig. S8(e and f) and Table S8 in the SI). In contrast, BCM-10% and BCM-15% follow pseudo-first-order kinetics where the $\ln(C/C_0)$ is well fitted by a linear equation and the C/C_0 reaction curves follow an exponential decay (Fig. S8(g–j) and Table S8). The order of the photo removal rate was as follows for the BCM composites: BCM-10% (0.0067 min^{-1}) > BCM-5% (0.0043 min^{-1}) > BCM-15% (0.0030 min^{-1}). Accordingly, BCM-10% not only featured the highest degradation percentage, but also the highest rate among the investigated materials.

Recycling test of BCM-10% (displayed in Fig. S9 in the SI) showed a fair performance retention (a decrease in CIP photodegration as high as 8% was recorded after 5 cycles), suggesting a good stability of the material under working conditions.

The materials discussed in this work showed a fairly good performance, compared with recently investigated BIOI composites applied in CIP photodegradation (a summary is provided in Table 5). However, the reader should be aware that a direct and reliable performance comparison is impaired by the different experimental conditions applied, as well as by different approaches in data analysis.

3.4. Investigating the catalytic material BCM-10%: scavenger analysis

To elucidate the photocatalytic mechanism of the BCM-10% composite, scavenger experiments were performed using *p*-benzoquinone (BQ), isopropanol (IPA), and KI as quenchers

Table 4 Results of the adsorption and photodegradation efficiency of the materials under investigation

Sample	% adsorption (120 min, light OFF)	% degradation (240 min, light ON)
BiOI	32.66	32.35
CAU-17	20.16	18.11
BC-10%	31.27	49.23
BC-20%	30.00	54.00
BC-30%	28.00	35.61
BCM-5%	32.38	63.58
BCM-10%	36.84	80.00
BCM-15%	46.90	55.76

Table 5 Comparison with recent literature using BiOI composited for the photodegradation of ciprofloxacin

Material	CIP initial concentration	CIP degradation	Ref.
BiOI-MOF-biochar	10 ppm	94.4% 180 min Simulated solar light	22
BiOI-polyurethane	20 and 40 ppm	~94% 12 h Visible light	55
$BiOIO_3$–Fe(III)	10 ppm	~91% 60 min Simulated solar light	56
BiOI/Bi_2WO_6	20 ppm	96% 80 min Visible light	57
BiOI-sulfate TiO_2	20 ppm	~86% 35 min Visible light	58
Fe-doped BiOCl/BiOI	10 ppm	95% 60 min Simulated solar light +12 V applied voltage	59
BiOI/$MnFe_{12}O_{19}$	20 ppm	~57% (pH 9) 200 min Simulated solar light	60
BiOI/MOF/MOP	10 ppm	80% 4 h Simulated solar light	This work

for $\cdot O_2^-$, ·OH, and photogenerated holes, respectively (Fig. S10, SI). The addition of all scavengers resulted in a decrease in CIP degradation, confirming the involvement of multiple reactive species. Among them, $\cdot O_2^-$ plays a dominant role, as evidenced by the significant drop in degradation efficiency from ~80% to ~30% upon the addition of BQ. Photogenerated holes also contribute substantially, with KI reducing the removal efficiency to ~50%. In contrast, IPA induces a less pronounced decrease, indicating a comparatively minor role of ·OH radicals under the investigated conditions.

These results suggest that CIP degradation proceeds *via* a complex mechanism primarily driven by superoxide radicals and holes, with hydroxyl radicals contributing to a lesser extent.

The kinetics of the reactions with BQ, IPA, and KI deviated from the pseudo-first-order, already obtained for the BCM-10% composite (fitting results shown in Fig. S11 and quantification reported in Table S9 in the SI). The deviation is dominant in the case of BQ, indicating the stronger influence of the superoxide anion radical on the kinetics. The reaction courses obeyed a sigmoidal model, indicating that autocatalytic reactions are occurring when the scavengers are added to the reaction mixture.

3.5. Investigating the catalytic material BCM-10%: the role of pH

We eventually investigated the role of pH in the photodegradation of CIP promoted by BCM-10%.

CIP behaves as a weak acid in water, due to the presence of a carboxylic function and an aminic group (carboxylic acid, pK_{a1} = 6.1, and amine in the piperazine ring, pK_{a2} = 8.7). This has important implications for the solubility and reactivity of the antibiotic in water, making it pH-dependent. CIP exists in the cationic form at pH <6.1, zwitterionic at pH in the range 6.1–8.7, and anionic at pH >8.7. The molecule is more stable at a pH of 4.0, where the carboxylic group is un-ionized, and the basic nitrogen is entirely protonated.[61]

The catalytic results analyzing the effect on different pHs on the CIP photodegradation are presented in Fig. 7. The photo-removal of CIP was drastically improved by increasing the pH from 3 to 11 and, remarkably, under strongly alkaline conditions (pH 11), the removal efficiency of CIP reached 100% after 120 min. In medium alkaline conditions (pH 9), the complete removal of CIP was as well achieved, but in a longer time (240 min).

Under acidic conditions, hydronium ion and CIP^+ compete to reach the catalyst's active sites and CIP adsorption on the photocatalyst surface is reduced (Fig. 8). On the contrary, the reaction between ·OH and CIP is accelerated in an alkaline medium: a high amount of OH^- supports the production of $^{\cdot}OH$, induced by photogenerated exciton pairs.[62–65]

Adsorption under dark was also profoundly affected by the pH (shown as reaction course in Fig. 8a) and the impressive adsorption at the equilibrium reached by the BCM-10% composite at pH 9 (Fig. 8b). While under sunlight irradiation a difference is clearly observed between pH 3 and pH 6.2, the pH played no role at all under dark. This finding calls for different depressed/enhanced photoexcitation of CIP depending on the pH,[66] which eventually affects its photocatalytic removal.

Although we could not measure the pH_{zpc} of our material, the influence of pH on CIP removal can be further interpreted on a qualitative basis by considering surface charge and pollutant speciation. It is reasonable to assume that the composite exhibits a pH_{zpc} in the near-neutral to slightly basic range, implying a positively charged surface under acidic conditions and a negatively charged surface in alkaline media. Under acidic conditions, the catalyst surface is likely protonated, and the high concentration of H^+/H_3O^+ competes with ciprofloxacin for active sites (also positively charged due to

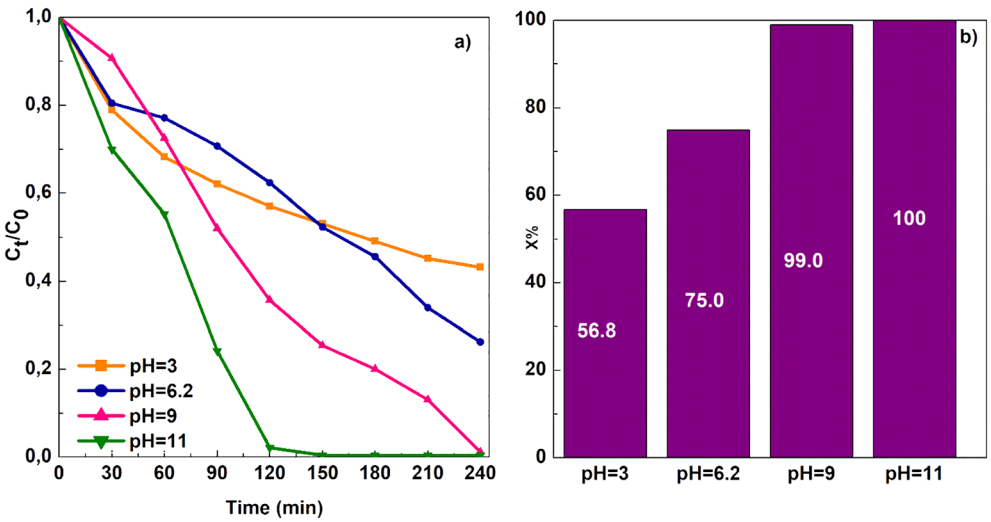

Fig. 7 Effect of pH on CIP photodegradation: a) reaction course plotted as C_t/C_0 and b) removal efficiency at different pHs after 240 min reaction.

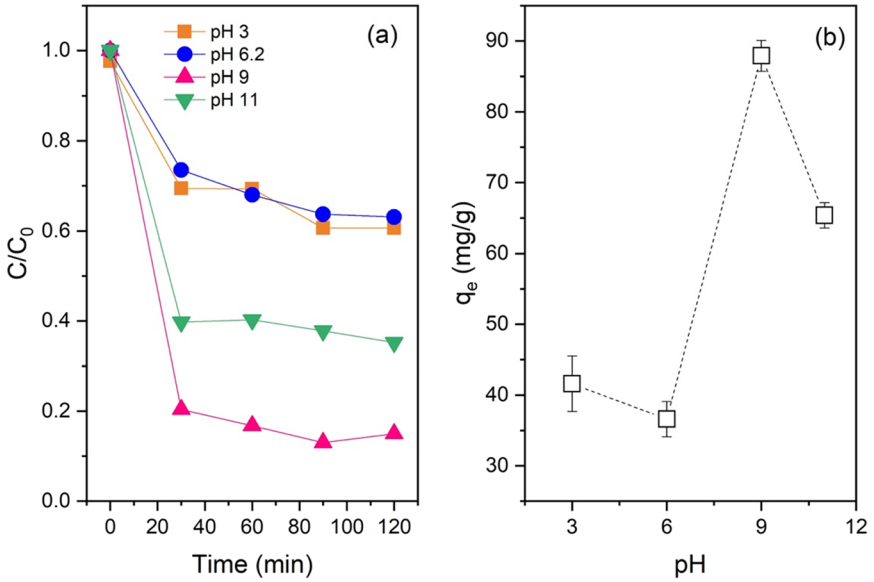

Fig. 8 (a) CIP adsorption under dark at different pHs. (b) Adsorption at the equilibrium as a function of pH.

the amino group), thereby suppressing adsorption and limiting interfacial charge transfer. In contrast, at higher pH values, deprotonation of the catalyst surface may enhance the interaction with CIP and facilitate electron transfer processes. Moreover, alkaline conditions promote the formation of reactive oxygen species, particularly ·OH and $\cdot O_2^-$, due to the increased availability of OH^- ions, which contributes to the observed enhancement in photocatalytic activity. This interpretation is consistent with the pH-dependent speciation of ciprofloxacin, which transitions from cationic to zwitterionic and finally to anionic forms with increasing pH, further influencing its interaction with the catalyst surface. While this analysis remains qualitative, it provides a coherent framework to rationalize the strong pH dependence observed in both adsorption and photocatalytic degradation.

3.6. HPLC-MS analysis

To try and identify the photodegradation pathway, the reaction mixtures where the ternary composite BCM-10% was used as the catalyst were analyzed by HPLC-MS (the results are shown in Fig. S13 in the SI). Possible degradation pathways, as previously identified in the literature, are reported in Scheme 1.[65,66]

Upon the adopted analytical conditions, CIP exits the column at a retention time (RT) of 4.06 min and its *m*/*z* spectrum consists of 3 peaks (Fig. S13a), ascribable to the parent ion M^+ (332.18) and a fragmentation proceeding through the elimination of the carboxylic function (*m*/*z* = 288.21) and the fluorine (*m*/*z* = 268.31).

The photodegradation of CIP generally occurs in the cyclopropyl group, carboxylic acid, piperazine ring, and F atom.[67,68]

The analysis of the reaction mixture at pH 3 (Fig. S13b), results in a single asymmetric peak in the chromatogram (RT = 2.34 min), showing a tail that is possibly due to the use of a C18 column. This suggests the presence of a single reaction product, more polar than CIP, whose most intense ion peak features a mass-to-charge ratio as high as 316, suggesting the loss of the fluorine atom and the rearrangement of the piperazine ring to give ethylene ciprofloxacin. This hypothesis is reasonable in acidic conditions, where both the –COOH and –NH groups present on CIP are protonated and fluorine is released to offer a higher stabilization of the overall charge.

At increasing pHs (Fig. S13c and d), the chromatogram still shows a single elution peak (RT at about 2.40 and 2.54 min for pH 6.2 and 9, respectively), which however appears as the overlap of more than one species, whose contributions we could not separate with our analytical setup. Mass spectroscopic analysis reveals the presence of the same reaction product in both mixtures, whose most intense ion peak is found at a mass-to-charge ratio of 288 (indicating the loss of the carboxylic function from CIP). It should be highlighted that we could not identify this reaction product for certain. However, in alkaline conditions, the carboxylic group may become more prone to an electrophilic attack and the molecule may undergo a McLafferty rearrangement, possessing an appropriately located oxygen bond to a π-system: this situation may rather well explain what is observed in the HPLC-MS analysis of the reaction mixtures at pH 9 and 11.

The C–N bond of the piperazine ring is the possible candidate for direct photo-hole oxidation. CIP adsorbs H_2O molecules and loses the piperazine ring that causes intermediates to form (*m*/*z* = 263). The product with *m*/*z* = 245 is generated *via* losing the fluorine atom (Scheme 1a, pathway 1).[69–73]

As shown in Scheme 1a, Pathway 2, CIP and its photocatalytic intermediates can be defluorinated. *M*/*Z* = 313 can be attributed to the loss of the fluorine atom, which is

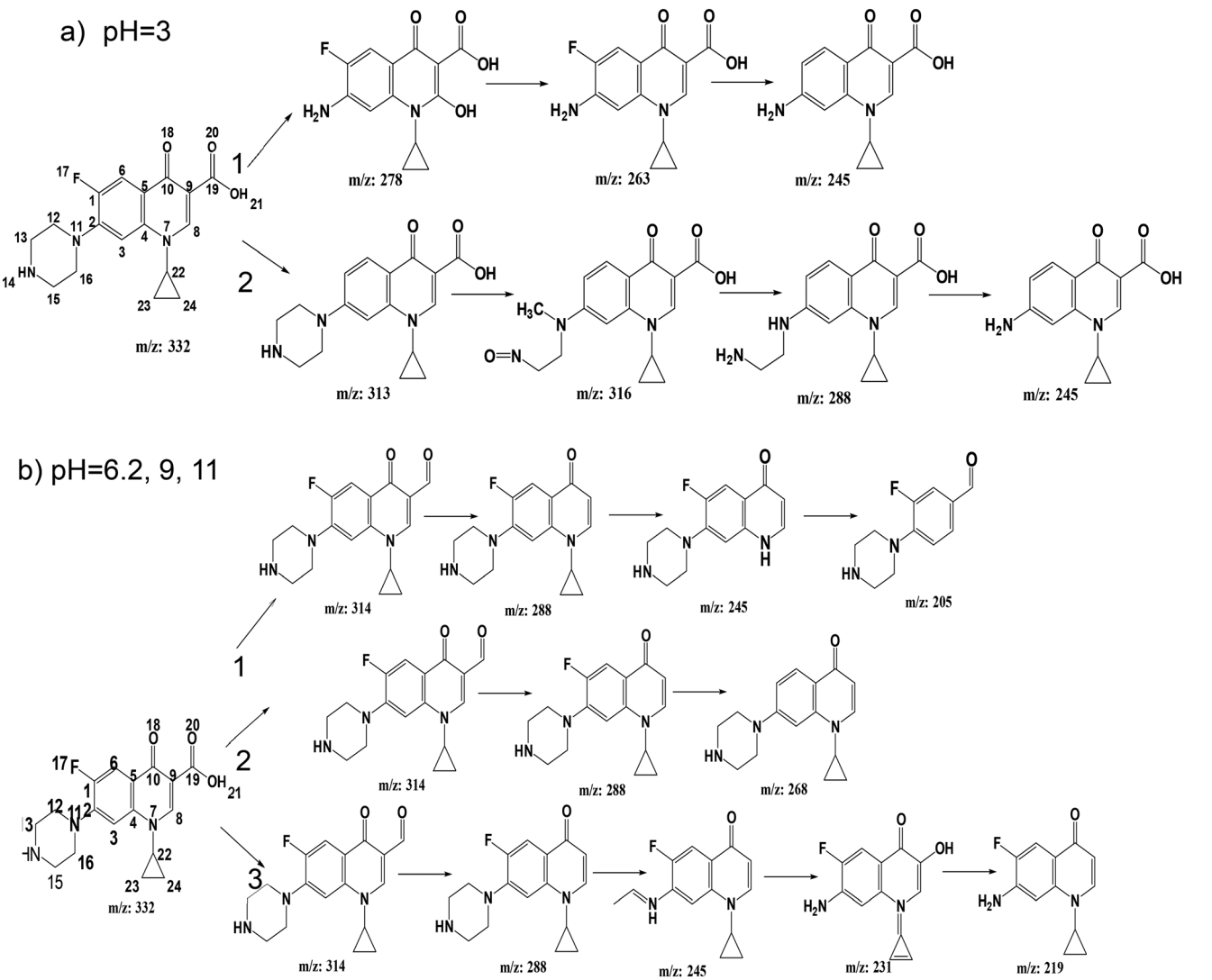

Scheme 1 Possible degradation pathways of CIP. (a) Acidic pH and (b) neutral water (pH 6.2 is induced by CIP autolysis) and alkaline conditions.

formed by the addition of the H_2O molecule and the breaking of the piperazine ring structure. Then, the aryl radicals produced by the loss of F and subsequent opening of the piperazine ring lead to the formation of (m/z = 316). The CN bond of the CIP piperazine ring is broken to give (m/z = 288), which is then converted to (m/z = 245). (m/z = 245) is the final transformation product of CIP in this pathway. $^{\bullet}O_2^-$ and H^+ are the essential species in breaking the piperazine ring.[70,74,75]

According to the HPLC-MASS results in pH = 6.2, 9, and 11, the mass (m/z) at 314, 288, 268, and 245 shows the most important intermediates which can respond to the removal of carboxylic acid, florin, and piperazine ring from the CIP. Other masses in trace values indicating fragments of main products are also detected as follows; 206, 219, 231, and 268 mass (m/z) (Fig. S13 in the SI). Three possible degradation pathways of CIP are suggested in Scheme 1b. This shows that photocatalysts are quite selective and that CIP degradation occurs by removal of the –COOH for all the materials (mass 288 (m/z)). In pathway 1, (m/z = 245) is produced by loss of the cyclopropyl group, which means that cleavage at cyclohexene in the quinolone moiety may occur in the intermediate m/z = 205. In pathway 2, m/z = 268 is formed by losing the fluorine atom.[76]

For pathway 3, at m/z = 332, the protonated CIP ion produces four major signals (m/z = 314, m/z = 288, m/z = 245, m/z = 231 respectively). The ion at m/z = 314 corresponds to dehydration, but the ion at m/z = 231 might have been produced by the loss of CO and diethylamine when the piperazine ring ruptured. The resultant ion is extremely unsaturated, and the double bond conjugation helps in ion charge delocalization. m/z = 219 can be generated by the dehydroxylation of CIP m/z = 231.[76]

4. Proposed mechanism

A mechanism for the removal of CIP is proposed in Scheme 2. Exciton pairs are produced upon exposure to simulated solar

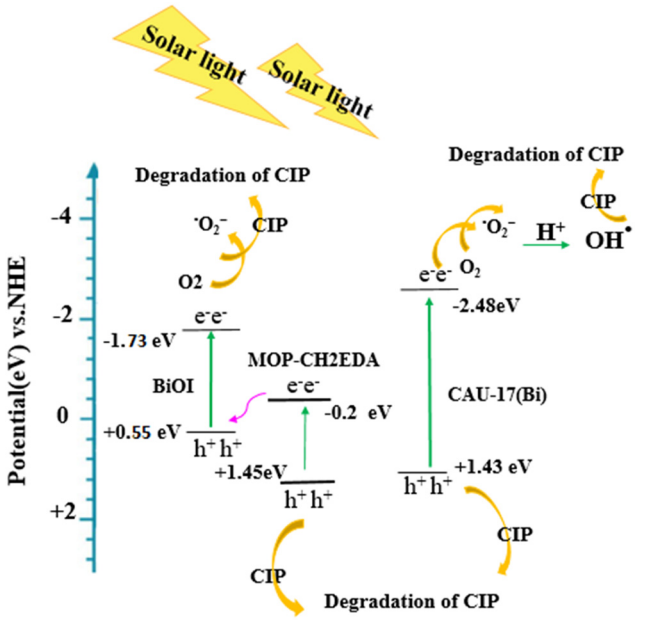

Scheme 2 Schematic diagram of the hypothesized charge transfer pathway for the ternary composite BCM-10% upon light irradiation.

light (CAU-17 is excited by UV light, while, BiOI and MOP-CH_2-EDA are active also in the visible). The possible photo carriers transfer mechanism (*i.e.*, Z-scheme method) are sketched.

The photoexcited electron in the CB of CAU-17 and BiOI can participate in reducing O_2 to $^{\bullet}O_2^-$ and then boosting CIP degradation. Meanwhile, the photogenerated electron in the CB of MOP-CH_2EDA (−0.2 eV), is not more negative than the $O_2/^{\bullet}O_2^-$ (−0.33 eV), and would swiftly be utilized by the holes generated in the VB of CAU-17 and BiOI. At the same time, the accumulated holes on the VB of CAU-17 and MOP-CH_2-EDA could directly oxide CIP molecules to produce small fragments. Nevertheless, the VB level of CAU-17 (+1.43 eV) and MOP-CH_2EDA (+1.45 eV) are less positive than $H_2O/^{\bullet}OH$ (2.73 eV *vs.* NHE), so photogenerated holes in the VB could not react with H_2O molecules and converted to the $^{\bullet}OH$. Moreover, the active $^{\bullet}O_2^-$ species could initiate reactions, and thus ·OH involve in the photodegradation reaction. As a result, the ternary composite is regarded as a critical factor for better photocatalytic degradation of CIP.

The estimated band positions are indeed consistent with a Z-scheme-like charge-transfer pathway in which the most reductive electrons remain on BiOI/CAU-17 to generate $\cdot O_2^-$, while the more oxidative holes are retained on the complementary component to oxidize CIP directly. However, the available band-edge estimates and scavenger tests support this assignment only indirectly, and the origin of ·OH should be treated cautiously.

5. Conclusions

This study demonstrates that the enhanced performance of BiOI/CAU-17/MOP-CH_2EDA composites arises from a coupled adsorption–photocatalysis mechanism, in which each component plays a distinct and interdependent role. Rather than acting independently, adsorption and photocatalysis are mechanistically linked: the MOP-CH_2EDA phase increases local ciprofloxacin (CIP) concentration through amine–π and electrostatic interactions, while the BiOI/CAU-17 heterostructure governs charge separation and reactive oxygen species (ROS) generation. Scavenger experiments indicate that $\cdot O_2^-$ is the dominant oxidizing species, supported by electron transfer from the conduction bands of BiOI and CAU-17, whereas photogenerated holes contribute directly to CIP oxidation and ·OH plays a secondary, pH-dependent role. The proposed Z-scheme-like charge transfer is therefore consistent with both the band alignment and the observed ROS hierarchy, although direct spectroscopic evidence of interfacial charge migration remains lacking.

Despite these improvements, the system exhibits several intrinsic limitations. First, the photocatalytic efficiency is strongly pH-dependent, with optimal performance under alkaline conditions, which may limit applicability in real wastewater matrices where pH control is impractical. Second, the coexistence of adsorption and photocatalysis complicates kinetic interpretation: the apparent pseudo-first-order behavior observed for ternary composites likely reflects a convolution of surface pre-concentration and reaction kinetics rather than a true intrinsic rate law. Third, the role of CAU-17 is ambivalent—while it contributes to heterojunction formation and charge separation, it simultaneously reduces pore accessibility and adsorption capacity, indicating a trade-off between transport and electronic effects. In addition, partial deactivation over reuse cycles suggests that surface fouling by intermediates or structural instability cannot be excluded. Finally, HPLC-MS analysis confirms multiple parallel degradation pathways, but the incomplete identification of intermediates prevents a rigorous assessment of mineralization efficiency and potential toxicity of by-products.

When critically compared with state-of-the-art visible-light photocatalysts, the BCM-10% composite shows moderate activity (≈80% CIP removal in 240 min), which remains inferior to optimized BiOI-based heterojunctions (*e.g.*, doped BiOI, BiOI/Bi_2S_3, or carbon-modified systems) that often achieve near-complete degradation within shorter irradiation times under similar conditions. This indicates that, although the present system benefits from multifunctionality, its charge separation efficiency and redox driving force are not yet fully optimized. In particular, the relatively weak oxidative potential of the valence bands limits ·OH generation, while recombination pathways—although mitigated—are not completely suppressed.

Overall, this work highlights that the primary advantage of BiOI/MOF/MOP composites lies not in maximizing intrinsic photocatalytic activity, but in enabling a synergistic process where adsorption governs mass transfer and interfacial concentration, and photocatalysis governs transformation pathways. Future progress should therefore focus on (i) decoupling and quantitatively distinguishing adsorption and reaction contributions, (ii) engineering stronger internal electric

fields or true Z-scheme architectures to enhance charge separation, and (iii) benchmarking under standardized conditions to enable meaningful comparison with advanced photocatalysts. Without such developments, multifunctional composites risk offering improved versatility at the expense of absolute performance.

Conflicts of interest

There are no conflicts to declare.

Data availability

The data supporting this article have been included as part of the supplementary information (SI).

Supplementary information: Fig. S1. XRD patterns of the materials under investigation. Table S1. Surface area and pore analysis of the prepared samples as retrieved from BET measurements. Fig. S2. Nitrogen adsorption–desorption isotherms for as-prepared materials. Fig. S3. FTIR spectra of the prepared materials. Table S2. IR correlation table. Fig. S4. Bi 4f photoemission spectra of the samples BiOI (a) and CAU-17 (b). Fig. S5. C 1s photoemission spectra of the samples (a) BiOI, (b) CAU-17 and (c) MOP-CH_2EDA. Table S3. XPS quantification tables with chemical state of the species for the samples BiOI. Table S4. XPS quantification tables with chemical state of the species for the sample CAU-17. Table S5. XPS quantification tables with chemical state of the species for the sample MOP-CH_2EDA. Fig. S6. XPS spectra of the composite BC-20%. Table S6. XPA quantification for the composite BC-20%. Fig. S7. XPS spectra of the composite BCM-10%. Table S7. XPS quantification of the composite BCM-10%. Fig. S8. Reaction course for the degradation of CIP upon light irradiation for pure CAU-17 (a and), BiOI (b and c) and the ternary composites (e–g). Markers are experimental points, lines are fitting curves. Table S8. Fitting parameters of plots, C_t/C_0 and $\ln C_t/C_0$ *vs.* time, for CIP degradation for pure BiOI, CAU-17, and the ternary composites. Table S7. XPS quantification of the composite BCM-10%. Fig. S8. Reaction course for the degradation of CIP upon light irradiation for pure CAU-17 (a and b), BiOI (b and c) and the ternary composites (e–g). Markers are experimental points, lines are fitting curves. Table S8. Fitting parameters of plots, C_t/C_0 and $\ln C_t/C_0$ *vs.* time, for CIP degradation for pure BiOI, CAU-17, and the ternary composites. Fig. S9. Recycling efficiency of the photocatalyst BCM-10%. Fig. S10. Results of the catalytic tests carried out with the addition of scavengers. (a) Reaction course plotted as C_t/C_0 *vs.* time and (b) degradation percentage as a function of the specific scavenger. Fig. S11. Reaction course for the degradation of CIP upon light irradiation for BCM-10%, and with the addition of different IPA, KI and BQ scavengers. Markers are experimental points, lines are fitting curves. Table S9. Fitting parameters of plots, C_t/C_0 and $\ln C_t/C_0$ *vs.* time, for CIP degradation with the addition of scavengers. For BCM-10% ternary composites. Fig. S12. Effect of pH on CIP photodegradation promoted by BCM-10%:(a) reaction course plotted as C_t/C_0 *vs.* time and (b) removal efficiency at different pHs after 240 min reaction. Fig. S13. Chromatograms and MS patterns pertaining to a) CIP and catalytic CIP degradation promoted by the ternary composite BCM-10% under simulated solar light at different pHs: b) pH = 3, c) pH = 6.2, d) pH = 9,11. See DOI: https://doi.org/10.1039/d6cy00135a.

Acknowledgements

The authors acknowledge the financial support for the project entitled "Purification platforms for the treatment of pharmaceutical wastes (no. SMK-1974)" from the Kempe Foundation. The Bio4Energy program is acknowledged.

References

1 I. O. Sanusi, G. O. Olutona, I. G. Wawata and H. Onohuean, *Environ. Sci. Pollut. Res.*, 2023, **30**, 90595–90614.
2 P. Barathe, K. Kaur, S. Reddy, V. Shriram and V. Kumar, *J. Hazard. Mater. Lett.*, 2024, **5**, 100105.
3 B. M. Al-howri, S. Ismail and M. Khajavian, *Environ. Monit. Assess.*, 2025, **197**, 1095.
4 J. R. Paulson, I. Y. Mahmoud, S. K. Al-Musharafi and S. N. Al-Bahry, *Open Biotechnol. J.*, 2016, **10**, 342–351.
5 N. S. Chauhan and A. Punia, in *Degradation of Antibiotics and Antibiotic-Resistant Bacteria from Various Sources*, ed. P. Singh and M. Sillanpää, Academic Press, 2023, pp. 179–201.
6 E. M. Cuerda-Correa, M. F. Alexandre-Franco and C. Fernández-González, *Water*, 2020, **12**(1), 102.
7 S. Li, Y. Wu, H. Zheng, H. Li, Y. Zheng, J. Nan, J. Ma, D. Nagarajan and J.-S. Chang, *Chemosphere*, 2023, **311**, 136977.
8 Q. Zhang, D. Zheng, B. Bai, Z. Ma and S. Zong, *Chem. Eng. J.*, 2024, **500**, 157134.
9 T. L. Wakjira, K. Tadele, A. B. Gemta and G. B. Kassahun, *Discover Mater.*, 2024, **4**, 56.
10 M. Arumugam, T. S. Natarajan, T. Saelee, S. Praserthdam, M. Ashokkumar and P. Praserthdam, *Chemosphere*, 2021, **282**, 131054.
11 S. Boochakiat, B. Inceesungvorn, A. Nattestad and J. Chen, *ChemNanoMat*, 2023, **9**, e202300140.
12 M. Long, P. Hu, H. Wu, Y. Chen, B. Tan and W. Cai, *J. Mater. Chem. A*, 2015, **3**, 5592–5598.
13 M. Arumugam and M. Y. Choi, *J. Ind. Eng. Chem.*, 2020, **81**, 237–268.
14 L. Huidobro, A. Domingo, E. Gómez and A. Serrà, *Chemosphere*, 2024, **366**, 143532.
15 F. Du, Z. Lai, H. Tang, H. Wang and C. Zhao, *Chemosphere*, 2022, **287**, 132391.
16 A. C. Mera, Y. Moreno, J. Y. Pivan, O. Peña and H. D. Mansilla, *J. Photochem. Photobiol., A*, 2014, **289**, 7–13.
17 X. Yang, X. Zhang, T. Wu, P. Gao, G. Zhu and J. Fan, *Colloids Surf., A*, 2020, **605**, 125344.
18 N. Talreja, S. Afreen, M. Ashfaq, D. Chauhan, A. C. Mera, C. A. Rodríguez and R. V. Mangalaraja, *Chemosphere*, 2021, **280**, 130803.

19 L. Huang, L. Yang, Y. Li, C. Wang, Y. Xu, L. Huang and Y. Song, *Appl. Surf. Sci.*, 2020, **527**, 146748.
20 F. Du, Z. Lai, H. Tang, H. Wang and C. Zhao, *Chemosphere*, 2022, **287**, 132391.
21 V. Vasanthakumar, M. Alsawalha, T. Alomayri, S. Allehyani, Y. b. Hu, M. L. Fu and B. Yuan, *Chemosphere*, 2022, **306**, 135505.
22 S. G. Khasevani, D. Nikjoo, C. Chaxel, K. Umeki, S. Sarmad, J.-P. Mikkola and I. Concina, *ACS Omega*, 2023, **8**, 44044–44056.
23 J. O. Eniola, R. Kumar and M. A. Barakat, *Environ. Sci. Pollut. Res.*, 2019, **26**(34), 34775–34788.
24 J. Dutta and A. A. Mala, *Water Sci. Technol.*, 2020, **82**, 401–426.
25 Z.-Y. Lu, Y.-L. Ma, J.-T. Zhang, N.-S. Fan, B.-C. Huang and R.-C. Jin, *J. Water Process Eng.*, 2020, **38**, 101681.
26 J. Song, L. Zhu, S. Yu, G. Li and D. Wang, *RSC Adv.*, 2024, **14**, 33489.
27 D. Mukherjee, J. Behera, S. Mondal, S. C. Pal, D. Volkmer and M. C. Das, *Cryst. Growth Des.*, 2023, **23**(11), 7612–7634.
28 C. Negro, H. M. Pérez-Cejuela, E. F. Simó-Alfonso, W. Iqbal, J. M. Herrero-Martínez, D. Armentano, J. Ferrando-Soria and E. Pardo, *ACS Appl. Mater. Interfaces*, 2023, **15**, 3069–3076.
29 F. Hooriabad Saboor, N. Nasirpour, S. Shahsavari and H. Kazemian, *Chem. – Asian J.*, 2022, **17**, e202101105.
30 N. Li, L. Huo, W. Shen, C. Qiang, M. Wu, G. Sun, Q. Li, M. Shi and J. Ma, *J. Cleaner Prod.*, 2023, **396**, 136558.
31 F. Wang, F. Ren, P. Mu, Z. Zhu, H. Sun, C. Ma, C. Xiao, W. Liang, L. Chen and A. Li, *J. Mater. Chem. A*, 2017, **5**, 11348–11356.
32 M. N. Alnajrani and O. A. Alsager, *Sci. Rep.*, 2020, **10**, 794.
33 S. Gholizadeh Khasevani and M. R. Gholami, *Mater. Res. Bull.*, 2018, **106**, 93–102.
34 W. Lu, J. P. Sculley, D. Yuan, R. Krishna, Z. Wei and H.-C. Zhou, *Angew. Chem., Int. Ed.*, 2012, **51**, 7480–7484.
35 F. Zhang, X. Xiao and Y. Xiao, *Dalton Trans.*, 2022, **51**, 10992–11004.
36 W. Fan, H. Li, F. Zhao, X. Xiao, Y. Huang, H. Ji and Y. Tong, *Chem. Commun.*, 2016, **52**, 5316–5319.
37 A. K. Inge, M. Köppen, J. Su, M. Feyand, H. Xu, X. Zou, M. O'Keeffe and N. Stock, *J. Am. Chem. Soc.*, 2016, **138**, 1970–1976.
38 M. Thommes and K. A. Cychosz, *Adsorption*, 2014, **20**, 233–255.
39 M. Thommes, K. Kaneko, A. V. Neimark, J. P. Olivier, F. Rodriguez-Reinoso, J. Rouquerol and K. S. W. Sing, *Pure Appl. Chem.*, 2015, **87**, 1051–1069.
40 N. Talreja, M. Ashfaq, D. Chauhan, A. C. Mera, C. A. Rodríguez and R. V. Mangalaraja, *New J. Chem.*, 2021, **45**, 18412–18420.
41 A. C. Mera, C. A. Rodríguez, M. F. Meléndrez and H. Valdés, *J. Mater. Sci.*, 2017, **52**, 944–954.
42 W. Tang, Y. Zhang, H. Guo and Y. Liu, *RSC Adv.*, 2019, **9**, 14060–14071.
43 Y. Wu, X. Song, S. Li, J. Zhang, X. Yang, P. Shen, L. Gao, R. Wei, J. Zhang and G. Xiao, *J. Ind. Eng. Chem.*, 2018, **58**, 296–303.
44 S.-R. Zhu, M.-K. Wu, W.-N. Zhao, P.-F. Liu, F.-Y. Yi, G.-C. Li, K. Tao and L. Han, *Cryst. Growth Des.*, 2017, **17**, 2309–2313.
45 Y. Xia, Z. He, J. Su, B. Tang, K. Hu, Y. Lu, S. Sun and X. Li, *RSC Adv.*, 2018, **8**, 4284–4294.
46 L. Yang, Y. Xin, C. Yao and Y. Miao, *J. Mater. Sci.: Mater. Electron.*, 2021, **32**, 13382–13395.
47 D. Dai, J. Qiu, M. Li, J. Xu, L. Zhang and J. Yao, *J. Alloys Compd.*, 2021, **872**, 159711.
48 Y. Li, X. Shang, C. Li, X. Huang and J. Zheng, *Water Sci. Technol.*, 2018, **77**, 1441–1448.
49 J. Rodriguez-Pereira, S. A. Rincón-Ortiz and R. Ospina, *Surf. Sci. Spectra*, 2020, **27**, 024001.
50 A. Bonilla-Petriciolet, D. Mendoza-Castillo and H. Reynel, *Adsorption Processes for Water Treatment and Purification*, 2017.
51 F.-C. Wu, R.-L. Tseng, S.-C. Huang and R.-S. Juang, *Chem. Eng. J.*, 2009, **151**, 1–9.
52 W. J. Weber and J. C. Morris, *J. Sanit. Eng. Div.*, 1963, **89**, 31–59.
53 J. Wang and X. Guo, *Chemosphere*, 2022, **309**, 136732.
54 Y. Liu, *Colloids Surf., A*, 2008, **320**, 275–278.
55 X. Wang, J. Zhang, G. Yu, Y. Wang, A. Zheng, Y. Cheng and S. He, *J. Environ. Chem. Eng.*, 2026, **14**, 121087.
56 S. Li, L. Chen, Z. Liu, M. Zhang, B. Li and C. Lai, *Appl. Surf. Sci.*, 2021, **566**, 150658.
57 X. Zou, S. Wang, C. Wu, Z. Peng and J. Yang, *J. Nanomater.*, 2022, **2022**, 5771628.
58 M. Khairy, M. M. Mohamed, K. A. Soliman, E. M. Masoud and M. Sameeh, *J. Environ. Manage.*, 2024, **370**, 123032.
59 S. Zheng, Z. Feng, J. Cheng and S. Han, *J. Environ. Chem. Eng.*, 2026, **14**, 120677.
60 M. Kargar, A. H. Hamidian and N. Nasseh, *Int. J. Environ. Sci. Technol.*, 2025, **23**, 121.
61 X. Hu, X. Hu, Q. Peng, L. Zhou, X. Tan, L. Jiang, C. Tang, H. Wang, S. Liu, Y. Wang and Z. Ning, *Chem. Eng. J.*, 2020, **380**, 122366.
62 K. Torniainen, S. Tammilehto and V. Ulvi, *Int. J. Pharm.*, 1996, **132**, 53–61.
63 S. Xing, W. Li, B. Liu, Y. Wu and Y. Gao, *Chem. Eng. J.*, 2020, **382**, 122837.
64 E. De Bel, J. Dewulf, B. De Witte, H. Van Langenhove and C. Janssen, *Chemosphere*, 2009, **77**, 291–295.
65 M. Sayed, M. Ismail, S. Khan, S. Tabassum and H. M. Khan, *Environ. Technol.*, 2016, **37**, 590–602.
66 T. An, H. Yang, G. Li, W. Song, W. J. Cooper and X. Nie, *Appl. Catal., B*, 2010, **94**, 288–294.
67 A. Salma, S. Thoröe-Boveleth, T. C. Schmidt and J. Tuerk, *J. Hazard. Mater.*, 2016, **313**, 49–59.
68 X. Mi, Y. Li, X. Ning, J. Jia, H. Wang, Y. Xia, Y. Sun and S. Zhan, *Chem. Eng. J.*, 2019, **358**, 299–309.
69 X.-J. Wen, C.-G. Niu, L. Zhang, C. Liang, H. Guo and G.-M. Zeng, *J. Catal.*, 2018, **358**, 141–154.
70 W. Li, S. Li, Y. Tang, X. Yang, W. Zhang, X. Zhang, H. Chai and Y. Huang, *J. Hazard. Mater.*, 2020, **389**, 121856.
71 F. Zhu, Y. Lv, J. Li, J. Ding, X. Xia, L. Wei, J. Jiang, G. Zhang and Q. Zhao, *Chemosphere*, 2020, **252**, 126577.

72 K. Liu, Z. Tong, Y. Muhammad, G. Huang, H. Zhang, Z. Wang, Y. Zhu and R. Tang, *Chem. Eng. J.*, 2020, **388**, 124374.
73 F. Chen, G.-X. Huang, F.-B. Yao, Q. Yang, Y.-M. Zheng, Q.-B. Zhao and H.-Q. Yu, *Water Res.*, 2020, **173**, 115559.
74 T. G. Vasconcelos, D. M. Henriques, A. König, A. F. Martins and K. Kümmerer, *Chemosphere*, 2009, **76**, 487–493.
75 Y. You, Z. Zhao, Y. Song, J. Li, J. Li and X. Cheng, *Sep. Purif. Technol.*, 2021, **258**, 117977.
76 H. Ou, J. Ye, S. Ma, C. Wei, N. Gao and J. He, *Chem. Eng. J.*, 2016, **289**, 391–401.